Hindawi
Advances in Materials Science and Engineering
Volume 2023, Article ID 9854589, 1 page
https://doi.org/10.1155/2023/9854589

Retraction

Retracted: Progress of Laser Processing Technology in Ferroelectric Nanocomposites

Advances in Materials Science and Engineering

Received 26 December 2023; Accepted 26 December 2023; Published 29 December 2023

This article has been retracted by Hindawi, as publisher, following an investigation undertaken by the publisher [1]. This investigation has uncovered evidence of systematic manipulation of the publication and peer-review process. We cannot, therefore, vouch for the reliability or integrity of this article.

Please note that this notice is intended solely to alert readers that the peer-review process of this article has been compromised.

Wiley and Hindawi regret that the usual quality checks did not identify these issues before publication and have since put additional measures in place to safeguard research integrity.

We wish to credit our Research Integrity and Research Publishing teams and anonymous and named external researchers and research integrity experts for contributing to this investigation.

The corresponding author, as the representative of all authors, has been given the opportunity to register their agreement or disagreement to this retraction. We have kept a record of any response received.

References

[1] H. Ding, Y. Fan, H. Dong, C. Zhao, and D. Zhao, "Progress of Laser Processing Technology in Ferroelectric Nanocomposites," *Advances in Materials Science and Engineering*, vol. 2022, Article ID 6502169, 12 pages, 2022.

Hindawi
Advances in Materials Science and Engineering
Volume 2022, Article ID 6502169, 12 pages
https://doi.org/10.1155/2022/6502169

Research Article

Progress of Laser Processing Technology in Ferroelectric Nanocomposites

Haijuan Ding, Yaping Fan, Hairong Dong, Chengtao Zhao, and Debiao Zhao

Shandong Provincial University Laboratory for Protected Horticulture, Weifang University of Science and Technology, Weifang 262700, Shandong, China

Correspondence should be addressed to Haijuan Ding; dinghaijuan@wfust.edu.cn

Received 7 September 2022; Revised 23 September 2022; Accepted 24 September 2022; Published 11 October 2022

Academic Editor: Haichang Zhang

Although polymer-based nanocomposites have great application potential in many fields, compared with the application of ferroelectric nanocomposites in functional microscale structures and devices, especially in the field of photonics microdevices fabricated by laser processing, the development of polymer-based nanocomposites is relatively lagging behind. In this study, the polyvinylidene fluoride ferroelectric composite material was taken as the research object, and the preparation method of polymer nanocomposite material suitable for laser microstructure processing was solved by exploring the material functionalization method. The control of the optical properties of polyvinylidene fluoride ferroelectric composites was achieved through material design, control of the size of nanoparticles in the prepared polymer nanocomposites, and characterization of their structures and properties. Two-dimensional and three-dimensional structures of polymer nanocomposites were prepared by laser microstructure processing technology, and the optical properties of the microstructures were evaluated. When the applied stress field was zero, the macroscopic coercive field was larger, and the hystereswas loop was wider, while the butterfly curve changed rapidly near the coercive field, and the strain was negative. From the test results of the scanning electron microscope, it can be concluded that the lowest average power to find ablation traces was 0.06 mw, and the affected area was very small, and there was no damage to the surrounding nanotubes. Therefore, this paper believes that the damage threshold of carbon nanotubes was slightly less than 0.06 mw. This study contributes to the development of nanocomposite preparation methods for laser micromachining.

1. Introduction

Smart material is a new type of functional material that can sense external (or internal) stimuli and make corresponding judgment and analyse processing. It is one of the key development directions of advanced material technology today. Based on these multifield coupling effects, many functions and physical effects of ferroelectric polymers can be realized. However, so far, the high-precision machining of ferroelectric nanocomposites is still dominated by traditional machining methods, which suffer from low machining accuracy, low efficiency, easy to produce machining defects, severe tool wear, high machining costs, and dust generated by machining and human health problems. For traditional electronic devices, the challenges they face are not only to further improve performance and reduce costs but also to develop towards miniaturization, portability, and intelligence. As a branch of electronic devices, ferroelectric devices must also meet the trend of scientific and technological development and begin to transform from traditional ceramic devices to thick film, thin film, and even molecular devices. This research is of great significance in the refined design of electronic devices.

Ferroelectric nanomaterials are favored by researchers because of their ability to realize multifield coupling effects between stress fields, electric fields, temperature fields, and optical fields. Wan C believed that energy harvesting utilized ambient energy sources, such as mechanical loads, vibrations, human motion, waste heat, light, or chemical sources, and converted them into useful electrical energy. He described examples of flexible harvesting devices utilizing optimized ferroelectric polymer or nanocomposite systems

and explored potential applications and future research directions [1]. A comparative study of the corresponding nanocomposites with BT nanoparticle fillers has been carried out by Li *Z* [2]. Zhang *J* believed that semicrystalline polymers accounted for more than half of all polymers produced globally. Their material properties were sensitively dependent on the thermal and flow history experienced during processing, which strongly affects the phase transition kinetics and morphology of the final crystalline microstructure [3]. A A Naberezhno investigated the internal structure of empty porous microporous and macroporous magnetic glasses and related nanocomposites containing $NaNO_2$ and KNO_3 embedded in the glass pores using small-angle neutron scattering [4]. In their study, the optical properties of ferroelectric nanomaterials were not discussed, so laser processing technology to optimize the ferroelectric nanomaterials were introduced.

Compared with the traditional technology, the surface microstructure forming technology based on laser processing has the advantages of good flexibility, high precision, low cost, and high efficiency, and it is easier to realize industrial production. Shen *X* aimed to introduce a method for fabricating microfluidic array chips with different pattern structures based on 248 nm excimer laser one-step etching. Through the comparative analysis of the graph neural network cultured on the microfluidic array chip and the graph neural network cultured on the glass slide, the influence of the neural network on the neuron morphology was studied [5]. Ferreira N *M* prepared MnO_3 precursors to produce fibers by using the laser floating zone technique [6]. Guangyi proposed a novel water-vapor shrinkage-guided high-power laser processing (WSLP) technique. First, the laminar flow and light guiding properties of the water-air coupling device were optimized. He studied the formation conditions of water-air laminar flow and their relationship [7]. Yan Y introduced a new one-step 3D printing technique for TE module fabrication that combined self-propagating high-temperature synthesis (SHS) with selective laser melting (SLM) methods [8]. By adjusting the laser processing parameters, single groove profiles with different depths and widths can be obtained, which will be further explored later.

This paper will focus on the ferroelectric, piezoelectric, and electrical properties of polyvinylidene fluoride ferroelectric polymers and systematically study the preparation process and the effect of blending modification (carbon-based nanoparticles) on the structure of polyvinylidene fluoride polymers. The influence of the performance and the controllable ferroelectric, piezoelectric, and electro-card properties of the polyvinylidene fluoride vinyl polymer is realized. This paper explored the technology of using laser to achieve high-efficiency and high-quality processing. Starting from the interaction process between the laser and high-modulus ferroelectric nanocomposites, based on experiments, the influence of various processing parameters on cutting quality is explored. To cut high modulus ferroelectric nanocomposites, the optimization of processing parameters is studied to achieve the cutting quality that meets requirements [9]. It is found that when the grafting rate was 26 wt%, the energy consumption rate of P(VDF-TrFE)-g-PMMA was about 20%. When the rolling temperature is lower than 60°C, the degree of damage to the lamellar structure is still relatively high, resulting in a long period of the sample, and the thickness of the lamellae and the thickness of the intermediate layer E decrease.

2. Application of Laser Processing Technology in Ferroelectric Nanocomposites

2.1. Ferroelectric Nanocomposites. Ferroelectric materials are materials with spontaneous polarization and two or more directions, which are widely used in various electronic devices. At present, according to the crystal structure, ferroelectric materials are mainly divided into four types: perovskite type, tungsten bronze type, lithium niobate type, and layered bismuth oxide structure. The polarization of ferroelectric materials changes due to the presence of an external electric field, and it changes with the change of the electric field. Under adiabatic conditions, by applying a fixed external electric field, the adiabatic temperature change and isothermal entropy change of the sample are as follows [10]:

$$\begin{aligned} \Delta T &= -T \int_{E_a}^{E_b} 1/\rho\,(\mu P/\mu T)dE, \\ \Delta S &= -T \int_{E_a}^{E_b} 1/\rho m_e F_t\,(\mu P/\mu T)dE, \end{aligned} \tag{1}$$

E_a and E_b are the initial and final electric fields, respectively.

The transition between seed crystal forms is shown in Figure 1. Considering the strong depolarization at the nanoscale, all lattices were designed in the range of several nanometers to several tens of nanometers, and the width of the lattices (the thickness of the structural bars of the lattices at nonintersections) was designed to be 6 nm. The ferroelectric material at the lattice structure strip is PVDF. The filling rate (the ratio of material occupied and the total area) of PVDF material is 30%. The crystallographic axis directions [100] and [010] of these two materials are parallel to the x and y axes, respectively. All models have periodic boundary conditions for electric potential and polarization in the x and y directions. To ensure stress freedom, all models do not set periodic boundary conditions for displacement. At the same time, displacement constraints were set in the x-direction of the left boundary node of the model and the y-direction of the lower boundary node of the model to avoid free translation of the model. Finally, in order to consider the effect of the depolarization field in the phase field model, except for the periodic boundary conditions (for example, the boundaries in the x and y directions), all the electrical boundary conditions on the surface of aperiodic materials were set to open circuits [11].

For optically isotropic dielectric materials, such as amorphous fused silica, BK7 glass, and so on, they are isotropic, so the nonlinear polarizability is scalar, and these materials have antisymmetric structures, so there was no second-order nonlinearity. Considering only the third-order nonlinear characteristics, the polarizability of the medium can be expressed as scalar [12], which is expressed as follows:

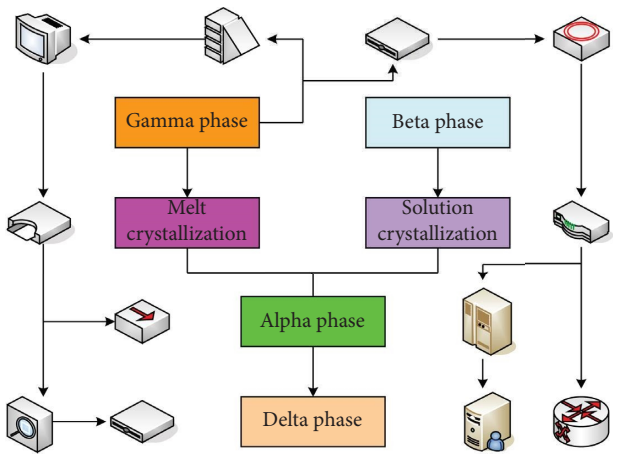

Figure 1: Transitions between different crystal forms.

$$P = \varepsilon_0\left(\chi_{(1)} + \chi_{(3)} \xrightarrow[|E|]{}\right)E. \tag{2}$$

When the content of filled nanoparticles is lower than the percolation threshold, the dielectric constant ε of the composite material will follow the following formula [13]:

$$\varepsilon = \left(\frac{\varepsilon_m f_c}{(1 - f_c)}\right) \bullet f_w. \tag{3}$$

ε_m represents the dielectric constant of the polymer matrix, and f_c refers to the percolation threshold [14].

When ferroelectric materials were used in pyroelectric devices, the figure of merit (FOM) was usually used as a parameter to characterize the detection performance of a ferroelectric material. However, according to different application scenarios, there are many merits to choose from. Usually the simplest figure of merit FOM is defined as follows:

$$\text{FOM} = \frac{p_f}{\varepsilon_w}. \tag{4}$$

ε_w represents the relative permittivity of the material [15].

2.2. Preparation and Experimental Materials of PVDF Films. The density of polyvinylidene fluoride (PVDF) used in the experiment is 1.75 g/cm^3. N-dimethylformamide (DMF) is chosen as the experimental solvent due to its strong polarity, and its density is 0.95 g/ml.

First, 0.3 g of PVDF powder was weighed and mixed with 5 ml of DMF reagent, and the magnet was added at room temperature for magnetic stirring for 24 h until PVDF was completely dissolved, and a colorless solution with a certain viscosity was obtained. Then, we take a syringe with a range of 5 ml to draw the solution, and we evenly drop it on a horizontal glass substrate with a size of 8 cm × 5.5 cm. Under the action of surface tension, a smooth and uniform liquid film was formed on the surface. Then, the glass plate was transferred to an oven at 60°C for 24 h. During this process, most of the DMF (an extremely versatile chemical raw material and an excellent solvent) solvent was volatilized, and the initial film was formed on the glass plate. Next, the glass plate was transferred to a vacuum oven and dried under vacuum at 75°C for 24 h to completely volatilize the residual DMF solvent in the initial film. The reason why it is necessary to volatilize the solvent in two steps without direct vacuum treatment is that the boiling point of DMF will drop significantly in vacuum. After the solvent was evaporated in vacuum, the film was peeled off from the glass plate, and the edge part was cut off for use. The initial film thickness of PVDF prepared by this process was about 40–50 μm. After obtaining the PVDF initial film completely free of DMF solvent, we cut it into several rectangular films with a length of 1.5–2.5 cm and a width of 1–1.5 cm, fix them on the fixture of the self-made pulling machine, and put them into a cylindrical furnace to preheat treatment for 1 h. Uniaxial stretching was performed at a certain rate, at a certain temperature, and at a certain speed. The whole preparation and stretching process is shown in Figure 2.

After the PVDF stretched film was prepared, in order to measure the FTIR (Fourier Transform Infrared Absorption Spectrometer) and hysteresis loop, the electrodes on both sides of the composite film were made by ion sputtering. In order to measure the pyroelectric coefficient of the sample, the sample needed to be polarized. The polarization process was as follows: we apply a DC electric field to the sample in silicone oil at 60°C; the polarization electric field was 70 MV/m, and the polarization time was 30 min. After polarization was completed, keep the electric field unchanged. After that, the samples were allowed to stand for one day, and then the pyroelectric coefficient was tested at a temperature range of 20–70°C and a heating rate of 2°C/min. The formula for calculating the β-phase content in the crystalline phase from the FTIR spectrum is as follows [16]:

$$F_\beta = C_\beta\left(1.33C_\alpha + C_\beta\right). \tag{5}$$

The formula for calculating crystallinity from a DSC curve is as follows:

$$x_N = \frac{\Delta H_m}{\left(1 - F_\beta\right)\Delta H_{m\alpha}^{-1} + F_\beta \Delta H_{m\beta}^{-1}}. \tag{6}$$

F_β was the relative content of the β phase, and ΔH_m was the melting enthalpy change of the composite [17].

2.3. Preparation of Polyvinylidene Fluoride Ferroelectric Nanocomposites. Before preparing the composites, multi-walled carbon nanotubes (MWNTs) were first subjected to hydrothermal oxidation treatment; 400 mg MWNTs were mixed with deionized water (40–50 g) and HNO3 (4–6 ml). After the hydrothermal reaction, the obtained product was repeatedly washed with deionized water, suction filtered, and finally freeze-dried to obtain oxidized MWNTs. The oxidized MWNTs were added to DMF and sonicated for about 2 h. Then, MWNTs/DMF was dropped into PVDF/DMF drop by drop. After the mixture was sonicated and vacuum stirred, the mixture was transferred to a clean glass substrate placed in a vacuum oven using a dropper and allowed to stand for 5 min to adjust the temperature of the

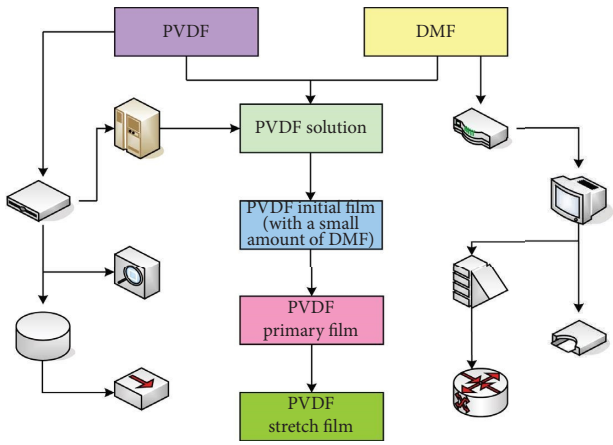

Figure 2: The entire fabrication and stretching process.

vacuum oven. At the holding time, the solvent volatilized to form a film. The film (thickness t_0: 100 μm) prepared by the solution crystallization method (solution-80°C) was cut into a rectangle with a length (a_0) of 2–6 cm and a width (b_0) of 2–6 cm. It was rolled parallel to the direction of a, the rolling temperature was about 50°C, the rolling rate was controlled between 20 and 30 r/min, the rolling elongation was 3.3, and the film thickness after rolling was 30 μm. The original and rolled composites were abbreviated as X and X-R, respectively, where X (0.05, 0.075, 0.1, 0.2, 0.3) represented the mass fraction of MWNTs corresponding to PVDF, and when X was 0, it was recorded as pure.

The phase field model of ferroelectric materials took polarization and strain as primary and secondary order parameters, respectively. The total energy density of ferroelectrics was expressed as follows [18]:

$$f = f_{\text{lan d}} + f_{\text{gra d}} + f_{\text{elec}}. \tag{7}$$

2.4. Establishment of the Laser Heat Source Model. The laser can process materials, mainly relying on its energy to deposit inside the material, making the material continue to heat up and even melt and vaporize. In an inert gas environment, the removal method of laser processing polyvinylidene fluoride ferroelectric nanocomposites was the degradation and vaporization of the resin matrix and carbon fiber [19]. Vaporization was carried out at high temperature, and vaporization removal was the main method, so in this simulation, when a unit reached its vaporization temperature, the unit should be removed, and heat flow was loaded to the unit below it. The interaction between the laser and the matter mainly depended on its thermal effect, so the laser can be loaded as a heat source. At the same time, due to the Gaussian distribution of laser energy within the beam radius r_0, the heat flux density formula can be obtained as follows [20]:

$$p(r) = p_n \exp(-Hr), \tag{8}$$

r was the distance between a point and the center of the spot.

Considering that the diameter of the laser spot was about 100 μm, the overall size of the model was set to 0.5 mm × 0.5 mm × 0.5 mm. Since the mass fraction of carbon fiber used was about 60%, the volume fraction of carbon fiber calculated according to the density of carbon fiber and resin was about 50%, so the carbon fiber tow was sized as a cylinder with a diameter of 40 μm. The heat flux density of the pulsed laser light source is as follows [21]:

$$q(r) = \frac{2P}{\delta r_1^2}\left(1 - \frac{2r^2}{\delta r_1^2}\right) + g(t),$$
$$g(t) = \begin{cases} 1, & (n-1)T < t < (n+1)T, \\ 0, & (n-1)T + \pi < t < nT. \end{cases} \tag{9}$$

In the formula, r_1 was the beam spot radius; P was the laser power (W); T was the period of the pulsed laser.

2.5. Laser Cutting Experiment. In this experiment, the cutting experiments of high-modulus polyvinylidene fluoride ferroelectric nanocomposites will be carried out for infrared lasers with a wavelength of 1064 nm and ultraviolet lasers with a wavelength of 355 nm. After cutting was completed, an ultrasonic cleaner was used to clean the residue on the surface of the workpiece [22]. Due to the Gaussian distribution of the laser beam, the width of the slit entrance was larger than the slit exit width during laser cutting, resulting in a certain taper of the slit. The calculation method of the slit taper in this study is as follows [23]:

$$T = \arctan\frac{W_t}{2d}. \tag{10}$$

T is the taper of the slit, and W_t is the width of the slit entrance.

The microhole processing of the ultrafast laser processing system was realized by the rotary scanning processing head. The rotary cutting scanning processing head was composed of a deflection optical wedge group, a translation optical wedge group, and a focusing mirror. Among them, the deflecting wedge group and the translation wedge group were composed of two small wedge angle and two large wedge angle wedges, each paired, and the two wedge groups could move independently. The variable diameter helical scanning process could be realized by adjusting the relevant parameters of the optical wedge group, and then the aperture and taper of the microhole could be adjusted. In actual processing, the rotary cutting scanning processing head sprays compressed air coaxially through the conical nozzle to remove the material slag produced during laser processing and improve the processing quality.

2.6. Performance Characterization

2.6.1. Electrical Performance Test. The hysteresis loops of the samples were tested by self-constructed Sawyer-Tower loops. When a pulse signal V is added to a resistor R for t time, the resistor will generate a Joule heat Q_h, which is expressed as follows:

$$Q_h = \left(\frac{V}{R}\right)t. \tag{11}$$

If the same heat flow sensor could sense the heat Q_{ECE} and Q_h that the sample releases or absorbs instantaneously when the electric field was applied or removed, the entropy change and temperature change of the material could be calculated according to the following two formulas:

$$\begin{aligned} Q_h &= Q_{ECE} = T\Delta H, \\ Q_{ECE} &= C_E \Delta T. \end{aligned} \tag{12}$$

Among them, CE represents the heat capacity of the material, which can be known by the DSC test.

2.6.2. Macroscopic Porosity Measurement. Before observing the surface quality of the material, the formed parts should be pretreated first: first, we put the forming square (10 mm × 10 mm × 5 mm) into the hot inlay machine, pour the inlaid material, melt and compact it, and cool it to obtain the inlaid sample; then, we use sandpaper and polishing cloth to grind and polish mosaic samples to ensure that no obvious scratches were observed with the naked eye; finally, we treat the mosaic samples to remove the contaminants brought in during the grinding process. The metallographic microscope Axiovert200MAT was used to observe the surface quality of composite materials. The magnification of the instrument was 50–1000 times. In this paper, 100 times of magnification was used for observation. Seven surface maps were randomly collected for each group of parameter samples, and the porosity value was calculated using Image-Pro Plus software, and then the maximum and minimum values were removed, and finally, the average porosity value of each group of samples was obtained. The relationship between relative permittivity and temperature is as follows:

$$\theta = \frac{(\theta_e + C)}{(T - T_0)}. \tag{13}$$

2.6.3. Mechanical Property Test. Before testing the hardness, the surface of the test sample should be ground and polished, and the upper and lower surfaces should be kept flat. In the process of measuring the hardness, the applied load and the load holding time were 1 kN and 15 s, respectively, and 7 different areas were selected for each group of parameter samples for dot measurement. After the experiment, 7 hardness values were obtained, and then the maximum and minimum values were removed to obtain the average hardness value of this group of samples.

The formula for the Bonn effective charge is as follows:

$$P_i = \frac{e}{\alpha_a} \sum_{j=1} w_j Z_j^* u_j. \tag{14}$$

The hysteresis loop and butterfly curve are the two main characteristics of ferroelectric materials and also the main characteristics of ferroelectric composite materials. Hysteresis loop and butterfly curve for ferroelectric composite measurement were measured. The basic circuit for measuring the hysteresis loop and butterfly curve is the Sawyer-Tower circuit. The principle of the Sawyer-Tower circuit is shown in Figure 3. C1 is the capacitance of the DUT (ferroelectric composite); C2 is a known capacitance, and $C2 >> C1$.

Measurement of electrical displacement: by measuring the electrical displacement, the hysteresis loop (an important characteristic parameter of ferroelectric thin films) of the ferroelectric composite material can be obtained so as to obtain very important parameters in the ferroelectric composite material, such as residual polarization P', coercive field E, and so on. The electrical displacement was obtained by measuring the change in the number of charges per unit area on the surface of the test piece. Since C1, C2 were in series, the charge on both capacitors was the same, that was $Q1 = Q2 = Q$. Therefore

$$\begin{aligned} \vartheta CV &= \theta CV = Q, \\ D &= \frac{Q}{A} = \frac{\epsilon \pi R^2}{A}, \end{aligned} \tag{15}$$

A is the effective area.

Measurement of electric fields: electric field strength is the potential difference per unit length. That is to say, the potential difference applied to the test piece is much larger than that applied to the known capacitance. Therefore, it is believed that the potential difference applied to the specimen is equal to the applied potential difference. From this, the electric field strength applied to the specimen can be obtained as

$$E = \frac{V}{H}. \tag{16}$$

H is the distance between the two surfaces of the specimen to which the electric field is applied.

Strain measurement: a strain gauge is attached to the surface of the specimen, the strain gauge and the temperature compensation sheet form a bridge, and the dynamic strain gauge is connected with the AD conversion circuit board to the computer, and the computer is used for sampling. While measuring the electric field and electric displacement, the longitudinal strain and transverse strain of the specimen are recorded.

Measurement of depolarization: depolarization is the 90° domain change of the ferroelectric phase in the ferroelectric composite under the action of compressive stress, resulting in a gradual decrease in the overall residual polarization of the ferroelectric composite. The mechanical and electrical coupling properties of the ferroelectric composites are reduced, and eventually, the ferroelectric composites do not show the mechanical and electrical coupling properties to the outside world. Coupling usually refers to the relationship between multiple circuits or power grids. In order to ensure that the ferroelectric composite specimen is subjected to pure compressive stress, a high-precision guide frame was designed, and the force sensor above the pressure rod was placed. In order to eliminate the influence of the parallelism

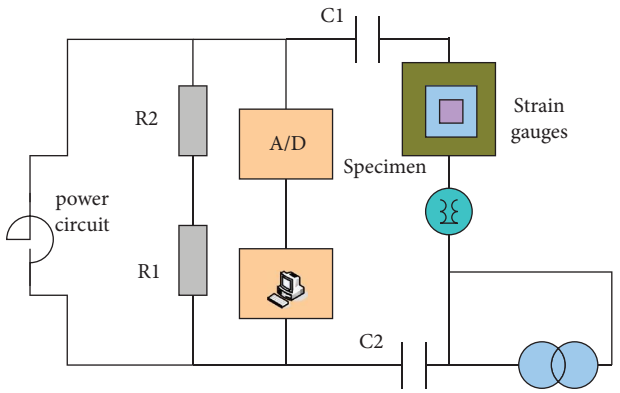

Figure 3: Sawyer-Tower circuit.

error of the upper and lower surfaces of the specimen on compressive stress, spherical indenters were used, which were placed on the upper and lower surfaces of the specimen, respectively. The test piece is the reference object and can be used as a reference for the value.

3. Results of Ferroelectric Nanocomposites

Based on the ferroelectric composite material model established in this paper, the electromechanical coupling problem of the ferroelectric composite material with PVDF material was calculated as the ferroelectric phase, and the volume percentage of PVDF was 95%. The material parameters used in the calculation are shown in Table 1. It is assumed that the elastic and dielectric properties of PVDF were isotropic, and the elastic and dielectric properties of the matrix were the same as those of PVDF.

It can be seen from Figure 4 that the calculated values are basically consistent with the experimental values. This shows that the model established in this paper can reflect the main properties of ferroelectric materials within a certain range. The difference between the calculation and the experiment is due to the assumption that the elastic and dielectric properties of the ferroelectric material are isotropic in the calculation and that the paraelectric-ferroelectric phase transition does not occur in 5% of the total volume of the material. From Figure 4, it can also be seen that when the applied stress field is zero, the macroscopic coercive field is larger, the hysteresis loop is wider, and the butterfly curve changes rapidly near the coercive field as well as the strain is negative. This is apparently due to the 90° domain change. With the increase of the applied compressive stress, the macroscopic coercive field gradually decreases, but the saturation electric field increases, which indicates that the electric domain inversion parallel to and opposite to the applied electric field becomes easier, while the electric domain at a certain angle to the electric field is easy to invert. Domain inversion becomes difficult. When the ferroelectric material with saturation polarization is subjected to an external compressive stress parallel to the polarization direction, the ferroelectric material will depolarize with the increase of the compressive stress. The saturation polarization in the article refers to the maximum value that the

Table 1: Material parameters used in calculations.

Material parameters	Numerical value
Young's modulus (MPa)	70
Poisson's ratio	0.22
Relative permittivity (farad/m)	6254
Piezoelectric coefficient d (m/V)	1652
Piezoelectric coefficient (m/V)	−602

polarization of ferroelectrics can reach when the applied electric field increases. These phenomena can be observed in experiments, which indicates that the theoretical model established in this paper can simulate the electromechanical coupling problem of ferroelectric materials well. Figure 4 shows the change of the electric field of the ferroelectric material when the applied stress is 0 MPa and −15 MPa.

From the analysis of Figure 5, it is seen that with the increase of the volume percentage of the ferroelectric phase, the electrical displacement of the ferroelectric composite increases significantly. In our experiment, the direction of the applied electric field is parallel to the three directions, that is, through the direction of the ferroelectric phase. From the analysis of the local field of the ferroelectric composite material in this paper, it can be seen that the local electric field applied to the ferroelectric phase and the applied electric field are completely consistent. In this case, the coercive electric field of the 1–3 type ferroelectric composite is the coercive electric field of the ferroelectric phase material, so no matter what the volume percentage of the ferroelectric phase inclusion is, the magnitude of the coercive field of the ferroelectric composites is the same, which can also be seen from the experimental results. The coercive field is a nonlinear relationship between polarization and the applied electric field. The large coercive field of ferroelectric composites is caused by the fact that the columnar inclusions of 28% of the specimens are not perpendicular to the upper and lower surfaces of the specimens. The relationship between the electric field and the electric displacement when the PVDF volume percentage is 14% and 28% is shown in Figure 5.

The hysteresis loop of the ferroelectric composite with PVDF as the matrix material is similar to the hysteresis loop of the ferroelectric composite with the matrix material of F-24, but the electric displacement value of the former is smaller than that of the latter, which is because the dielectric relaxation properties of PVDF are much smaller than that of F-24. It can be clearly seen from Figure 6 that the domain transition (domain change means electrical domain reversal) of the ferroelectric phase in the ferroelectric composite has an effect on the hysteresis loop of the ferroelectric composite. The properties of the matrix material have a great influence on the ferroelectric composites. For the ferroelectric composites whose matrix material is F-24, with the increase of the volume percentage of the ferroelectric phase, the residual electric displacement of the ferroelectric composites also increases. The experimental and calculated results are not in good agreement. The experimental curve of the ferroelectric composite with F-24 matrix has no obvious coercive stress, but the theoretical calculation does. The reason for this

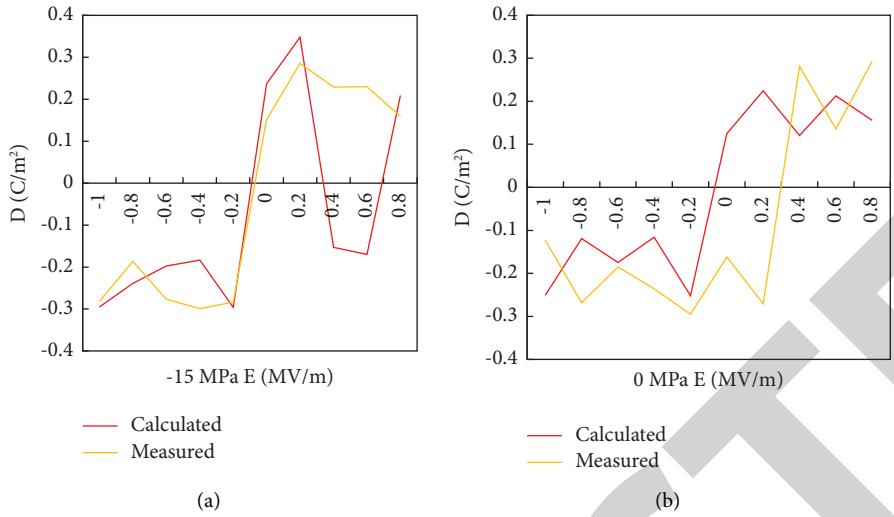

Figure 4: Changes in the electric field of ferroelectric materials when the applied stress is 0 MPa and −15 MPa.

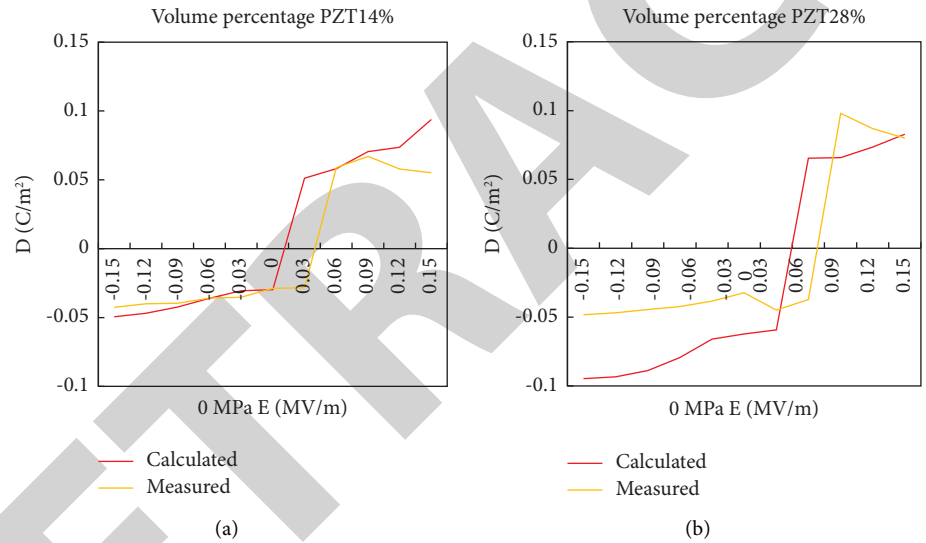

Figure 5: Relationship between electric field and electric displacement for PZT volume percentages of 14% and 28%.

difference may be that we did not consider the viscoelastic properties of the matrix in the calculation. The dielectric relaxation properties of F-24 are very strong, so its viscoelastic properties may also be very strong. For PVDF with weak dielectric relaxation properties, its viscoelastic properties may also be weak, so it can be seen from Figure 5 that there is a significant coercive stress in the piezoelectric curve of PVDF. From this analysis, it is believed that in the design and analysis of ferroelectric composites based on polymers, the influence of the viscoelastic properties of the matrix and the dielectric relaxation effect on the ferroelectric composites should be carefully considered. The effect of hysteresis loops of ferroelectric composites at loading amplitudes 6 and 9 is shown in Figure 6.

$N = 1$: the laser begins to ablate the material, and no ripples appear due to the single pulse; $N = 5$: parallel ripples begin to appear in the ablation area, and ripple spacing is about 739 nm. The Gaussian distribution curves are consistent, and the deepest part can reach 130.7 nm; $N = 10$: vertical ripples and parallel ripples still exist in the middle of the ablated region. The two kinds of corrugations are nearly orthogonal, and the width of the vertical corrugations is wider than the first one, with a width of about 1.45 μm, and the depth is deeper than the first one, with a depth of about 198 nm; $N = 50$: the vertical corrugations are gradually destroyed, and the middle ablation holes appear, the depth of the holes is about 670 nm, and the depth of the holes gradually deepens with the increase of the pulse number. The surface ripples formed at the edge of the material damage area are caused by laser scattering, interference, diffraction, and thermal deformation mechanisms. Diffraction is the physical phenomenon in which a wave deviates from the original straight line when it encounters an obstacle. The experimental phenomena and period values are in good agreement with the interference theory of scattered waves and incident waves. That is, when the laser irradiates the

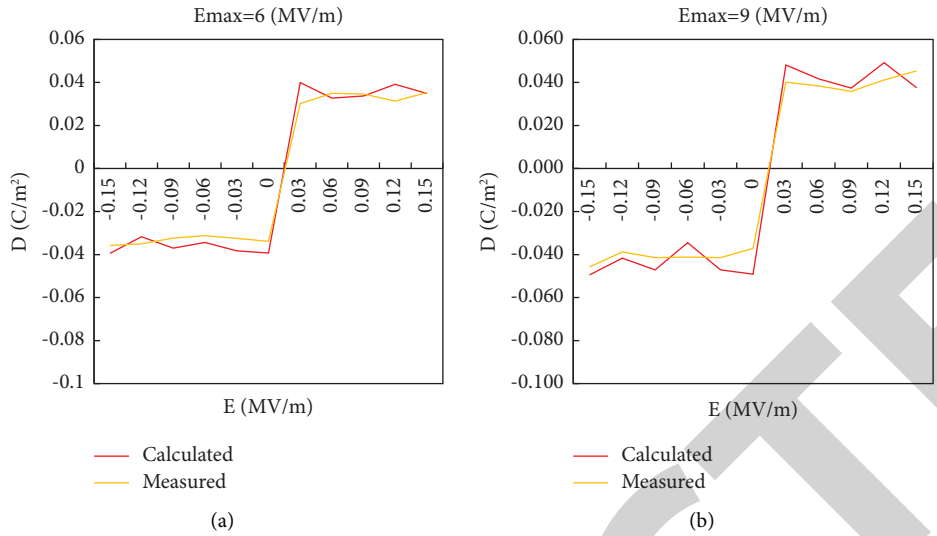

Figure 6: Effect of hysteresis loops of ferroelectric composites at loading amplitudes 6 and 9.

surface of the material, due to the influence of the surface roughness, a scattered wave will be generated, which will interfere with the incident laser, and the interference ripple will propagate along the surface, causing the periodic structure of the material surface. Through the discussion of the characteristics of corrugation and the formation process, several laws can be drawn: the femtosecond laser irradiation energy should be near the value of the interaction between the laser and the material, and excessive energy will directly destroy corrugation; multiple pulses act on the surface of the material to generate ripples. There is no similar ripple formation in a single pulse; under certain conditions, after the initial surface ripple is formed, the laser has a positive feedback effect on the growth of the ripple. This has a positive effect on the fabrication of a wide range of grating structures. The AFM test results are shown in Figure 7.

According to the test results of the scanning electron microscope, the lowest average power that can find ablation traces is 0.06 mw, the effect area is very small, and there is no damage to the surrounding nanotubes. Therefore, it can be determined that the damage threshold of carbon nanotubes is slightly less than 0.06 mw. Only a few carbon nanotubes on the surface were blown off. In the pictures of holes ablated by different laser energies, the number of burned carbon nanotubes can be roughly estimated so that the relationship between the average laser pulse power and the number of burned carbon nanotubes can be established visually. Laser pulses are characterized by good monochromaticity, small divergence, and high brightness. Although this is only a qualitative estimate, it has certain significance in actual processing. From this, it is not difficult to draw the conclusion that with the increase of the average power of the femtosecond laser, the number of blown carbon nanotubes shows a trend of linear increase. This is basically in line with what we predicted. The number of broken nanotubes at different powers is shown in Figure 8.

The tip of CNTs (carbon nanotubes) has a nanoscale curvature and can emit a large number of electrons at a relatively low voltage. Therefore, carbon nano-metal field emission is a kind of potential barrier that relies on a strong external electric field to suppress the surface of the object, reducing the height of the potential barrier and narrowing the width of the potential barrier, and a large number of electrons in the object escape through the surface potential barrier. The tube material can show good field emission characteristics, which is very suitable for the cathode of various field emission devices. The emission current of a single carbon nanotube can reach more than 1 μA after applying an electric field. Electrons can only move along the axial direction of the carbon nanotube in the single-layer graphite sheet, and the radial motion is limited, that is, the wave vector is axial. The electrical properties of partially opened CNTs are significantly better than those of closed carbon tubes, and it has been verified that femtosecond laser can process single CNTs, so opening the top of CNTs can be used as a new application of femtosecond laser micronano processing. In addition, using the characteristics of femtosecond laser processing, it is envisaged that the two ends of the incision of a single carbon tube are used as the emission end (cathode) and the receiving end (anode) of electrons, the incision distance is controlled at 1–5 μm, and the voltage is only 5–30 V (the field emission electric field strength of carbon nanotubes is 1–5 V/us), and if it is possible to be less than 1 μm, it can be made into a field emission device in the tunnel emission mode. The size of the turn-on voltage is controlled by the distance between the cuts, and then the I/V characteristic curve similar to a semiconductor diode is obtained under vacuum. The overall cut is shown in Figure 9. A single CNT was deposited on the groove of the metal layer, then cut with a laser, and then moved to a vacuum chamber to test the IV value.

The dielectric constants of several common polymers are shown in Table 2. In contrast, the dielectric constant of polymer materials is generally lower than that of ceramic materials. For example, despite its low dielectric constant (2.2), due to its extremely high breakdown strength

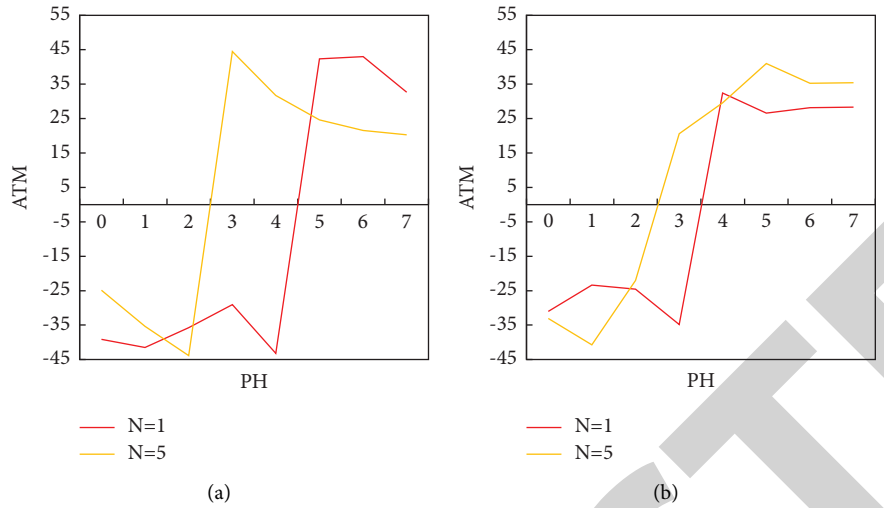

Figure 7: AFM test results.

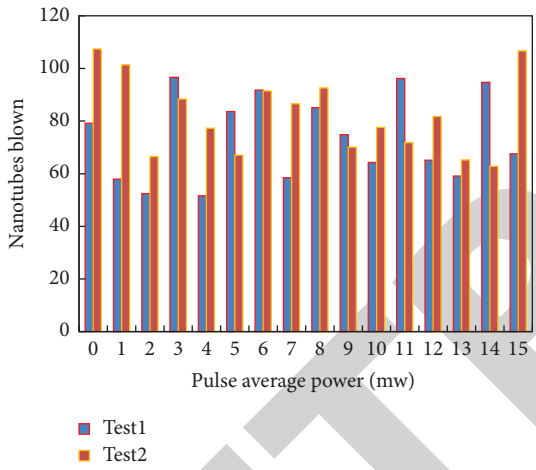

Figure 8: The number of burnt nanotubes at different powers.

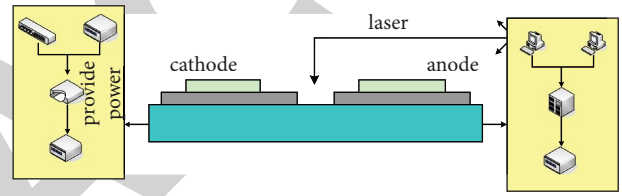

Figure 9: Overall cut.

Table 2: Dielectric constants of several common polymers.

Polymer	Dielectric constant	Breakdown strength (kV/mm)
Polypropylene (PP)	2.4	>500
Polyester (PET)	1.3	>400
Polycarbonate (PC)	2.8	>300
Polyimide (PI)	2.3	<400
Polyvinylidene fluoride (PVDF)	2.4	<500

(>600 kV/mm), the energy storage density of PVDF (polyvinylidene fluoride) film capacitors can still reach 1–2 J/cm^2 (0.3–0.6 Wh/kg) and almost no energy loss during charge-discharge cycles. At present, many PVDF-based dielectric capacitors are widely used in pulsed power devices in civil and military fields due to their high power density and energy storage capacity.

In order to compare the smoothness of the microstructured surface, SCR500 (an air compressor) was used to control the light intensity and exposure time to prepare the corresponding 2D microstructures. When CdS nanoparticles were doped into the polymer, the content of the crosslinking agent decreases, and CdS nanoparticles affected the regular arrangement of polymer chains, thus affecting the smoothness of the microstructure surface. The microstructure processing conditions of the ferroelectric nanocomposites are shown in Table 3.

When the external electric field is 50–100 MV/m, the energy consumption rate of each sample increases rapidly, especially at the energy consumption rate of pure sample as high as 80%, which is due to the high reversal energy barrier of the dipole, resulting in a large amount of ferroelectric losses. With the increase of the grafting rate, due to the nanoconfinement of PMMA, the size and content of the ferroelectric phase of the system gradually decrease, coupling between the ferroelectric domains weakens, dipoles are more easily flipped under the action of an external electric field, and the energy consumption rate gradually decreases. When the grafting rate is 26 wt%, the energy consumption rate of P(VDF-TrFE)-g-PMMA is only about 20%. The energy consumption rates at different grafting rates are shown in Figure 10.

The excellent ferroelectric properties of PVDF benefit from the high content of β-phase. Although the β-phase structure can be directly generated by low-temperature solution crystallization, the low solution crystallization temperature will cause the material to have a loose and porous structure, resulting in poor electrical properties of the material. However, when PVDF materials are prepared by the melt method, PVDF tends to crystallize directly to

Table 3: Microstructure processing conditions of ferroelectric nanocomposites.

Numbering	Film thickness (um)	Exposure time (s)
1	1.0	22
2	1.5	15
3	2.0	10
4	1.0	26
5	3.0	18

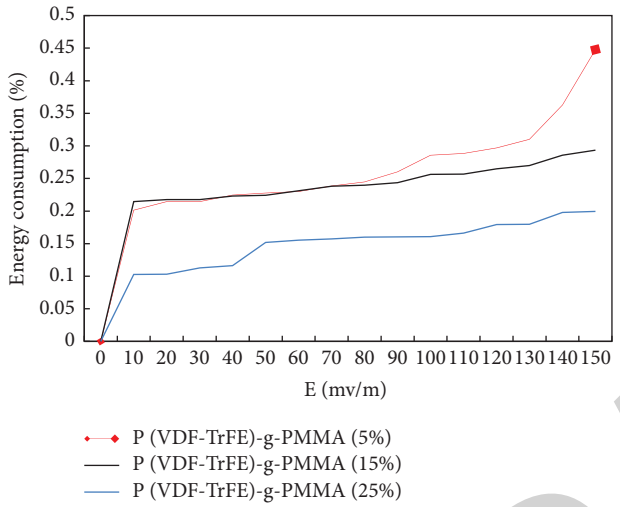

Figure 10: Energy consumption rates at different grafting rates.

form a more stable α-phase structure. The piezoelectric properties of piezoelectric polymers are compared in Table 4. The α phase is a low-temperature stable phase, and the β phase is a high-temperature stable phase.

Ferroelectrics have critical properties near the Curie transition point, which is of great significance for their practical applications. However, since the Curie temperature of PVDF exceeds its melting temperature, the ferroelectric-paraelectric phase transition cannot be observed within the effective operating temperature range of PVDF, which greatly limits the application range of PVDF ferroelectrics. However, the introduction of the second monomer can reduce the Curie temperature of the material below its melting temperature, and the Curie transition can occur within its effective operating temperature range. Taking P(VDF-TrFE) binary polymer as an example, its Curie transition can be observed below its melting temperature. The addition of TrFE (trifluoroethylene) enlarges the volume of the unit cell, making the molecular chain conformation susceptible to temperature-induced transformation, so the local temperature is lower than that of PVDF. Moreover, the Curie temperature of the binary polymer can be regulated by adjusting the content of TrFE. When the content of TrFE is higher than 20 mol%, the Curie transformation point is observed below the melting temperature of the binary polymer, and the Curie transformation temperature decreases with the increase of TrFE content. Near the Curie transition point, P(VDF-TrFE) undergoes the transformation from ferroelectric phase to

Table 4: Piezoelectric properties comparison of piezoelectric polymers.

Numbering	PVDF	P(VDF-TrFE)
PC/N	0.21	0.19
Electromechanical coupling coefficient	0.12	0.11
Maximum operating temperature (°C)	89	89

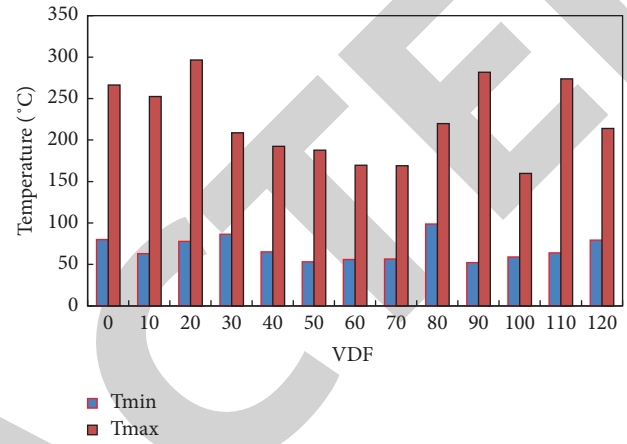

Figure 11: Ferroelectric-paraelectric phase structure transition induction.

paraelectric phase, and the large difference in lattice constant between the two phases will lead to a large hysteresis strain. It is worth noting that when the TrFE content is 50 mol%, the Curie temperature of the material reaches the lowest value of 60°C, and the further increase of TrFE content can no longer reduce the Curie temperature, so P(VDF-TrFE) cannot be Curie phase transition (the phase transition temperature caused by the transition of a ferroelectric phase from a ferroelectric phase to a paraelectric phase) at room temperature or at the temperature region near room temperature, and then some functions such as the large hysteresis stretching effect can be realized. The induction of ferroelectric-paraelectric phase structure transition is shown in Figure 11.

Under the action of external stress, the lamellae in the polymer will first slip, and then the lamellae structure will be destroyed, and the polymer molecular chain will recombine and start the recrystallization process. In this experiment, the rolling temperature is lower than 60°C. At this low temperature, the damage degree of the lamellar structure is high, resulting in the long period of the sample, and the thickness of the lamellar and the thickness of the intermediate layer E decrease. In addition, the reduction of rolling temperature will be unfavorable to the movement of molecular chains and the transfer of stress, local stress concentration is prone to occur inside the polymer, the degree of damage to platelets is higher, and the movement activity of polymer molecular chains is low, which is not easy to recombine. Therefore, the thickness of lamellae in the material decreases gradually with the decrease of rolling temperature. The E values of PVDF samples corresponding to different rolling temperatures are shown in Table 5.

Table 5: E values of PVDF samples at different rolling temperatures.

Sample	Rolling temperature (°C)	Mesophase interlayer thickness E(nm)
Original	25	1.1
1	30	0.22
2	35	0.34
3	40	0.35

4. Conclusion

In this study, the in-situ synthesis method of nanoparticles in polymers was adopted as the basic method, and a general method of polymer nanocomposites suitable for laser microstructure processing was developed through molecular design and material design of polymerized monomers. Polymer nanocomposites is an emerging discipline involving inorganic, organic, materials, physics and many other disciplines. Although polymer-based nanocomposites have huge potential applications in many fields and have become a hot spot in functional materials research today, compared to the application of polymer-based nanocomposites to functional microscale structures and devices, especially the use of lasers in the field of processing and preparing photonics microdevices, its research and development are lagging behind. Although polymer-based nanocomposites can be prepared by many methods, there are few methods for preparing polymer-based nanocomposites suitable for laser microstructuring. The size, distribution, and morphology of nanoparticles in the related polymer nanocomposites need to be studied, and the potential application of polymer nanocomposites in the field of laser micromachining needs to be further expanded. The performance of polymer nanocomposite microstructure still needs to be further improved to finally realize the preparation and application of functional microdevices based on polymer nanocomposites.

Data Availability

The data that support the findings of this study are available from the corresponding author upon reasonable request.

Conflicts of Interest

The authors declare that there are no conflicts of interest regarding the publication of this article.

Acknowledgments

This work was supported in part by the Talent Special Project of Weifang University of Science and Technology (2019RC004) and Shandong Provincial University Laboratory for Protected Horticulture Program (2018YY045).

References

[1] C. Wan and C. R. Bowen, "Multiscale-structuring of polyvinylidene fluoride for energy harvesting: the impact of molecular-, micro- and macro-structure," *Journal of Materials Chemistry*, vol. 5, no. 7, pp. 3091–3128, 2017.

[2] Z. Li, F. Liu, and G. Yang, "Enhanced energy storage performance of ferroelectric polymer nanocomposites at relatively low electric fields induced by surface modified BaTiO_3 nanofibers," *Composites Science and Technology*, vol. 164, pp. 214–221, 2018.

[3] J. Zhang, F. W. Zhao, Z. H. Liu et al., "Influence of core–shell structured conductive fillers on the electromechanical properties of ferroelectric nanocomposites," *Journal of Materials Science*, vol. 56, no. 15, pp. 9157–9170, 2021.

[4] A. A. Naberezhnov, V. Ryukhtin, and A. A. Sysoeva, "Internal structure of magnetic porous glasses and the related ferroelectric nanocomposites," *Physics of the Solid State*, vol. 59, no. 2, pp. 378–384, 2017.

[5] X. Shen, Y. Yang, S. Tian, Y. Zhao, and T. Chen, "Microfluidic array chip based on excimer laser processing technology for the construction of in vitro graphical neuronal network," *Journal of Bioactive and Compatible Polymers*, vol. 35, no. 3, pp. 228–239, 2020.

[6] N. M. Ferreira, A. R. Sarabando, M. C. Ferro, M. A. Madre, O. J. Dura, and A. Sotelo, "Tuning thermoelectric properties of Ca0.9Gd0.1MnO3 by laser processing," *Journal of Materials Science: Materials in Electronics*, vol. 31, no. 21, pp. 18913–18922, 2020.

[7] G. Zhang, Z. Zhang, Y. Wang, C. Guo, and W. Zhang, "Gas shrinking laminar flow for robust high-power waterjet laser processing technology," *Optics Express*, vol. 27, no. 26, pp. 38635–38644, 2019.

[8] Y. Yan, W. Geng, J. Qiu et al., "Thermoelectric properties of n-type ZrNiSn prepared by rapid non-equilibrium laser processing," *RSC Advances*, vol. 8, no. 28, pp. 15796–15803, 2018.

[9] A. A. Elngar and S. E. El-Dek, "A novel artificial face mask based nanofibers with special intelligent engineered nanocomposite against covid-19," *Journal of Cybersecurity and Information Management*, vol. 5, no. 2, pp. 21-22, 2021.

[10] L. J. Zhang, H. B. Zhang, X. W. Lei et al., "Laser processing of Mg-10Li-3Al-3Zn alloy:Part II- Improving corrosion resistance of multi-phase Mg alloys by laser surface processing," *Journal of Manufacturing Processes*, vol. 56, no. 5, pp. 571–580, 2020.

[11] P. Hauschwitz, R. Bicistova, J. Radhakrishnan, J. Brajer, and D. Rostohar, "Superhydrophobic stainless steel surface by two-step NS laser processing," *MM Science Journal*, vol. 2019, no. 05, pp. 3647–3651, Article ID 2019116, 2019.

[12] V. N. Popov and A. N. Cherepanov, "Optimization of modifying material distribution during laser processing of the metal surface," *Izvestiya Vysshikh Uchebnykh Zavedenii, Chernaya Metallurgiya*, vol. 60, no. 7, pp. 505–511, 2017.

[13] J. Zehetner, G. Vanko, J. Dzuba, and T. Lalinsky, "Femtosecond laser processing of membranes for sensor devices on different bulk materials," *Advances in Electrical and Electronic Engineering*, vol. 15, no. 3, pp. 561–568, 2017.

[14] S. Kou, Y. Gao, Y. Zhao, and B. Lin, "Stress analysis and optimization of Nd:YAG pulsed laser processing of notches for fracture splitting of a C70S6 connecting rod," *Journal of*

Mechanical Science and Technology, vol. 31, no. 5, pp. 2467–2476, 2017.

[15] C. Liu, M. Zhang, and C. Chen, "Effect of laser processing parameters on porosity, microstructure and mechanical properties of porous Mg-Ca alloys produced by laser additive manufacturing," *Materials Science and Engineering A*, vol. 703, pp. 359–371, 2017.

[16] Z. S. Hou, Q. L. Huang, X. P. Zhan, A. W. Li, and H. L. Xu, "Real 3D microsphere lasers by femtosecond laser processing," *RSC Advances*, vol. 7, no. 27, pp. 16531–16534, 2017.

[17] B. H. Babu, M. Niu, T. Billotte et al., "Femtosecond laser processing induced low loss waveguides in multicomponent glasses," *Optical Materials Express*, vol. 7, no. 10, pp. 3580–3590, 2017.

[18] J. Lichovník, Š. Malotová, and J. Zelinka, "Effect of laser processing parameters on cut quality after engraving," *Technological Engineering*, vol. 16, no. 1, pp. 11–15, 2019.

[19] O. C. Ann, F. S. Tee, and V. Y. Nen, "A study on satisfaction level among amateur web application developers towards pigeon-table as nano web development framework," *Journal of Organizational and End User Computing*, vol. 31, no. 3, pp. 97–112, 2019.

[20] B. N. Nyushkov, A. V. Ivanenko, and S. V. Smirnov, "Control of the regimes and parameters of lasing in mode-locked fiber lasers: opportunities and prospects," *Optoelectronics, Instrumentation and Data Processing*, vol. 57, no. 6, pp. 569–583, 2022.

[21] J. Coroado, S. Williams, W. Suder, S. Ganguly, S. Meco, and G. Pardal, "New phenomenological model for comparison of lasers with different temporal outputs," *International Journal of Advanced Manufacturing Technology*, vol. 120, no. 9-10, pp. 6107–6123, 2022.

[22] X. Cao, J. Xia, X. Meng, J. Xu, Q. Liu, and Z. Wang, "Stimuli-responsive DNA-gated nanoscale porous carbon derived from ZIF-8," *Advanced Functional Materials*, vol. 29, no. 34, Article ID 1902237, 2019.

[23] K. M. Nagaraja, W. Li, D. Qian, V. Vasudevan, Y. Pyun, and H. Lu, "Multiphysics modeling of in situ integration of directed energy deposition with ultrasonic nanocrystal surface modification," *International Journal of Advanced Manufacturing Technology*, vol. 120, no. 7-8, pp. 5299–5310, 2022.